Monthly Notices of the ROYAL ASTRONOMICAL SOCIETY

MNRAS **511,** 1408–1419 (2022) https://doi.org/10.1093/mnras/stac145
Advance Access publication 2022 January 27

The far-infrared/radio correlation for a sample of strongly lensed dusty star-forming galaxies detected by *Herschel*

M. Giulietti [1,2]★ M. Massardi,[1,3,4] A. Lapi,[1,3,5,6] M. Bonato,[3,4] A. F. M. Enia [2,7] M. Negrello,[8] Q. D'Amato,[2,7] M. Behiri[1] and G. De Zotti [9]

[1]*SISSA, Via Bonomea 265, I-34136 Trieste, Italy*
[2]*INAF – Osservatorio di Astrofisica e Scienza dello Spazio, Via Gobetti 93/3, I-40129, Bologna, Italy*
[3]*INAF/IRA, Istituto di Radioastronomia, Via Piero Gobetti 101, I-40129 Bologna, Italy*
[4]*INAF, Istituto di Radioastronomia – Italian ARC, Via Piero Gobetti 101, I-40129 Bologna, Italy*
[5]*INFN – Sezione di Trieste, via Valerio 2, Trieste 34127, Italy*
[6]*IFPU – Institute for fundamental physics of the Universe, Via Beirut 2, I-34014 Trieste, Italy*
[7]*University of Bologna – Department of Physics and Astronomy 'Augusto Righi' (DIFA), Via Gobetti 93/2, I-40129 Bologna, Italy*
[8]*School of Physics and Astronomy, Cardiff University, The Parade, Cardiff CF24 3AA, UK*
[9]*INAF, Osservatorio Astronomico di Padova, Vicolo Osservatorio 5, I-35122 Padova, Italy*

Accepted 2022 January 16. Received 2022 January 14; in original form 2021 September 22

ABSTRACT

We investigate the radio/far-infrared (FIR) correlation for a sample of 28 bright high-redshift ($1 \lesssim z \lesssim 4$) star-forming galaxies selected in the FIR from the *Herschel*-ATLAS fields as candidates to be strongly gravitationally lensed. The radio information comes either from high sensitivity dedicated Australia Telescope Compact Array observations at 2.1 GHz or from cross-matches with the FIRST survey at 1.4 GHz. By taking advantage of source brightness possibly enhanced by lensing magnification, we identify a weak evolution with redshift out to $z \lesssim 4$ of the FIR-to-radio luminosity ratio $q_{\rm FIR}$. We also find that the $q_{\rm FIR}$ parameter as a function of the radio power $L_{1.4\,\rm GHz}$ displays a clear decreasing trend, similarly to what is observed for optically/radio-selected lensed quasars found in literature, yet covering a complementary region in the $q_{\rm FIR}$–$L_{1.4\,\rm GHz}$ diagram. We interpret such a behaviour in the framework of an *in situ* galaxy formation scenario, as a result of the transition from an early dust-obscured star-forming phase (mainly pinpointed by our FIR selection) to a late radio-loud quasar phase (preferentially sampled by the optical/radio selection).

Key words: gravitational lensing: strong – quasars: general – galaxies: star formation – radio continuum: galaxies – submillimetre: galaxies.

1 INTRODUCTION

For several decades the rest-frame 1.4 GHz radio luminosity density $L_{1.4\rm GHz}$ (W Hz^{-1}) emitted by bright dusty star-forming galaxies has been associated with their far-infrared (FIR) luminosity $L_{\rm FIR}$ (8–1000 μm rest frame) in terms of an empirical relation between these two quantities, namely the *FIR–radio correlation* (Helou, Soifer & Rowan-Robinson 1985; Yun, Reddy & Condon 2001). Such a relation is found to be roughly linear across ∼3 orders of magnitude in luminosity $9 \lesssim \log(L_{\rm FIR}/{\rm L}_\odot) \lesssim 12.5$ with a rather low 1σ scatter $\lesssim$0.26 dex; it is often described via the parameter $q_{\rm FIR}$ (e.g. Yun et al. 2001; Magnelli et al. 2015) defined as

$$q_{\rm FIR} = \log\left(\frac{L_{\rm FIR}[{\rm W}]/3.75\times10^{12}}{L_{1.4\,\rm GHz}[{\rm W\,Hz^{-1}}]}\right). \quad (1)$$

The tightness of this relation can be ascribed to the common origin of the radio and FIR emissions as interpreted by *calorimetric* models (Lacki & Thompson 2010). In this framework, galaxies are assumed to be optically thick to the UV light coming from young new born stars, which is absorbed by the dust in the interstellar medium and then re-radiated in the FIR regime. At the end of their lives, the same massive stars explode as Type II supernovae producing cosmic ray electrons and positrons, radiating most of their energy in the radio band through synchrotron emission before escaping the galaxy. Additionally, a secondary component of the radio emission comes from the free–free contribution originated by the hot and ionized H II regions.

The FIR-radio correlation is well established in the local universe (Helou et al. 1985; Yun et al. 2001; Jarvis et al. 2010; Smith et al. 2014; Molnár et al. 2017; Wang et al. 2019). Its apparent tightness encouraged the use of radio emission as an unbiased tracer of obscured star formation in dusty galaxies (Kennicutt & Evans 2012), and prospectively as a probe to obtain a comprehensive view of the cosmic star formation history up to very high redshift (Madau & Dickinson 2014; Delhaize et al. 2017; Novak et al. 2017). This is, in fact, one of the key science drivers of the SKA and of its pathfinder telescopes such as ASKAP and MeerKAT (e.g. Jarvis et al. 2015) and of the next-generation Very Large Array (ngVLA), focused on the investigation of the emission mechanisms

★ E-mail: mgiuliet@sissa.it

that power the radio continuum emission in galaxies (Murphy 2019).

For example, early science data at 1.3 GHz from the MeerKAT International GHz Tiered Extragalactic Exploration (MIGHTEE; Jarvis et al. 2016) survey have been recently analysed in An et al. (2021), together with VLA and GMRT radio data, to investigate the radio spectral properties and the FIRRC for a sample of 2094 SFGs in the COSMOS field. Moreover, future observations with SKA will enable detailed investigations of magnetic fields in galaxies, which can be particularly relevant in the FIRRC especially in the low star formation rate (SFR) regimes (Schleicher & Beck 2016).

To achieve this goal, however, it is necessary to set on a firm basis the connection between radio and FIR emission (hence star formation), and to assess its redshift dependence, which has been strongly debated in last decades. From a theoretical perspective, an evolution in redshift is expected as a consequence of either the additional energy losses of the cosmic rays interacting with the cosmic microwave background photons through inverse Compton scattering (e.g. Murphy 2009; Lacki & Thompson 2010) or because of the co-evolution of AGNs in dusty environments with ongoing star formation in the early stages of galaxy evolution (Lapi et al. 2018). In fact, sources whose radio emission is dominated by nuclear activity show up as outliers of the FIR–radio correlation (Sopp & Alexander 1991; Stacey et al. 2018). A $q_{\rm FIR} = 1.8$ was proposed by Condon, Cotton & Broderick (2002) as the boundary between star formation and (radio-loud) AGN-dominated radio emission.

From an observational point of view, the evolution is far from being settled. On the one hand, different works found no significant evidence of a trend with redshift (e.g. Sargent et al. 2010). On the other hand, several authors pointed out the presence of a slight decline of the $q_{\rm FIR}$ parameter: Magnelli et al. (2015) report evidence of a weak redshift evolution in a mass-selected sample of galaxies, rendered as $q_{\rm FIR} \propto (1+z)^{-0.12\pm0.04}$; a similar result was found by Basu et al. (2015) for a sample of blue cloud galaxies at $z \leq 1.2$; Tabatabaei et al. (2016) studied the radio continuum emission from the KINGFISH sample of nearby galaxies finding that the FIR to 1–10 GHz luminosity ratio could decrease with the star formation rate, suggesting a decrease of the ratio at high redshifts where mostly luminous/star-forming galaxies are detected; more recently, Ocran et al. (2020) analysed the radio properties of 1685 star-forming galaxies selected at 610 MHz with the GMRT, inferring an evolution $q_{\rm FIR} \propto 2.86 \pm 0.04(1+z)^{-0.20\pm0.02}$ up to $z \sim 1.8$; Delhaize et al. (2017) found $q_{\rm IR} \propto (1+z)^{-0.19\pm0.01}$ for galaxies selected with the VLA at 3 GHz; Calistro Rivera et al. (2017) obtained $q_{\rm FIR} \propto (1+z)^{-0.15\pm0.03}$ for a sample of star-forming galaxies obtained with Low Frequency Array (LOFAR) at 150 MHz.

This observed evolution would imply that high-z ($z \gtrsim 1$) star-forming galaxies present somehow a more pronounced radio emission (or a lower FIR luminosity) compared to their local counterparts. Other studies instead argued on the possibility that the observed trend with the redshift may be a consequence of selection effects (e.g. Sargent et al. 2010; Bourne et al. 2011; Molnár et al. 2021), which can be ascribed to the difference in depth between radio and FIR surveys and to flux-limited samples or to selections biased towards more massive galaxies, as recently reported by different authors (Delvecchio et al. 2020; Bonato et al. 2021; Smith et al. 2021). In fact, investigations at higher redshifts, carried out up to $z \gtrsim 2$ (Ivison et al. 2010a; Thomson et al. 2014; Magnelli et al. 2015), have been limited by the availability of very deep radio data and/or redshift measurements. In this sense, selection biases can be minimized in homogeneous populations of FIR/submm galaxies (e.g. Algera et al. 2020). In fact, FIR/submm surveys are poorly affected by dust obscuration and feature almost constant flux densities across a wide range of redshifts ($0 \lesssim z \lesssim 10$, Blain et al. 2002). The resulting strong negative *K*-correction allowed the detection of such a population pre-dominantly at high redshifts ($z \sim 2$–3) up to $z \sim 6$. It has also become clear that the nuclear activity has a crucial impact on the host galaxy and its interstellar medium through the action of energy/momentum feedback (i.e. radio jets), affecting the scatter of the FIR-radio correlation (Sopp & Alexander 1991) and (probably) its redshift evolution. In this sense, the study of dusty star-forming galaxies in the (sub)mm and radio bands is crucial to characterize the interplay between nuclear activity and star formation; high$-z$ dusty galaxies are however compact, with typical intrinsic sizes of a few tenths of an arcsec (Pantoni et al. 2021), hence very hard to resolve.

In recent years, a big step forward has been made thanks to large-area submm surveys which have been used to efficiently select strongly lensed galaxies at high redshift. Lensing enables the observation of regions in the luminosity-redshift space of these sources that would be otherwise unattainable with current instrumentation or would require an excessive amount of integration time. Indeed, the magnifications of apparent luminosity and angular size by the effect of a foreground lens, offer the unique possibility of studying down to sub-kpc scales the properties of objects otherwise not exceptionally bright, massive, or peculiar, and belonging to the bulk of the galaxy population at the peak of the cosmic star formation history ($z \sim 2$, Madau & Dickinson 2014). In FIR/submm bands, high-z lensed dusty galaxies are particularly bright, while a negligible signal comes from the foreground lens, which is often a massive evolved elliptical at $z \lesssim 1$. Also the obscuration from the foreground lens that limits the investigation of the background galaxy in the optical is negligible in the FIR/submm domain.

The capabilities of the *Herschel* Space Observatory to select dusty star-forming lensed galaxies have been amply proved. Wardlow et al. (2013) identified 11 lensed galaxies over the 95 deg^2 of the *Herschel* Multi-tiered Extragalactic Survey (HerMES; Oliver et al. 2012); other 77 candidate lensed galaxies were found by Nayyeri et al. (2016) in the HerMES Large Mode survey (HeLMS; Oliver et al. 2012) and in the *Herschel* Stripe 82 Survey (HerS; Viero et al. 2014). The *Herschel* Astrophysical Terahertz Large Area Survey (H-ATLAS; Eales et al. 2010) is the widest area (600 deg^2) extragalactic survey undertaken by *Herschel* and has provided a sample of more than a hundred thousand dusty galaxies at high redshift. During the Science Demonstration Phase (SDP), covering a 16 deg^2 portion of the sky, Negrello et al. (2010) selected the first sample of five strongly lensed galaxies in H-ATLAS. Negrello et al. (2017) further exploited this survey to extract a catalogue of 80 candidate strongly lensed dusty star-forming galaxies brighter than 100 mJy at 500 μm.

In this paper, we present the radio properties of 28 *Herschel*-ATLAS candidate strongly lensed, dusty star-forming galaxies at redshifts $1 \lesssim z \lesssim 4$ extracted from the original sample by Negrello et al. (2017) (see Section 2). The radio data have been obtained as the result of the cross-matches with the FIRST survey at 1.4 GHz and of dedicated follow-up at 2.1 GHz with the Australia Telescope Compact Array (ATCA). We then derive the FIR–radio correlation, its redshift evolution, and its luminosity dependence (see Section 3). We compare our result to that of the lensed quasar sample by Stacey et al. (2018), highlighting the complementarity of the two selections and presenting a physically motivated interpretation in the framework of an *in situ* galaxy evolution model (see 4). Finally, we summarize our findings (see Section 5).

In this work, we adopt the standard flat ΛCDM cosmology (Planck Collaboration VI 2020) with rounded parameter values: matter density $\Omega_M = 0.32$, dark energy density $\Omega_\Lambda = 0.63$, baryon

density $\Omega_b = 0.05$, Hubble constant $H_0 = 100h$ kms^{-1}Mpc^{-1} with $h = 0.67$, and mass variance $\sigma_8 = 0.81$ on a scale of 8 h^{-1} Mpc.

2 THE SAMPLE

2.1 The H-ATLAS-lensed galaxies

Negrello et al. (2017) extracted a sample of 80 bright FIR/submm-selected galaxies with flux density $S_{500\,\mu m} > 100$ mJy from the H-ATLAS fields. The SPIRE photometry is obtained from the point-source *Herschel*/SPIRE catalogues of the H-ATLAS Data Release 1 and 2, described in Valiante et al. (2016) and Maddox et al. (2017). The catalogues have been created identifying the 2.5σ peaks in the SPIRE 250 μm maps, which are then used as position priors to measure flux densities in the other SPIRE bands. The instrumental and confusion noise have been minimized through the use of a matching filter for the creation of the maps from which fluxes have been extracted. Only sources with a signal-to-noise ratio >4 in at least one of the three SPIRE bands have been included in the final catalogue. As described in Negrello et al. (2017), extended sources have been detected through optical images and treated as contaminants, therefore are not included in the sample of 80 candidate lensed galaxies. The sample galaxies feature FIR (8–1000 μm) luminosities in the range $13 \lesssim \log(L_{\rm FIR}/L_\odot) \lesssim 14$ (uncorrected for lens magnification). They span a redshift range $1 \lesssim z \lesssim 4.5$ (29 spectroscopic, 51 photometric redshifts) with a median value $z_{\rm med} = 2.5$. However, to date, only 21 of the 80 candidates in Negrello et al. (2017) sample have been confirmed to be genuine strongly lensed objects through detailed optical/near-infrared (with *HST* and Keck) or submm (with SMA) images of their structure, together with spectroscopic redshift measurements of the background lensed galaxy and of the foreground lens. For other eight sources, the lensing scenario is strongly supported by the redshift difference of optical/NIR and submm galaxies along the line of sight. The remaining sources are classified as uncertain because they still miss proper follow-up that could confirm their lensed nature.

Some of the sources in the sample have been individually studied in detail exploiting multiwavelength high-resolution observations. For example, Enia et al. (2018) performed lens modelling and source reconstruction for 13 of the 500 μm-selected lensed galaxies in H-ATLAS using high-resolution SMA observations at 870 μm (Bussmann et al. 2013). SDP.81 has been the target of observations and modelling in the ALMA long-baseline campaign (Dye et al. 2015; Hatsukade et al. 2015; Partnership et al. 2015; Swinbank et al. 2015; Tamura et al. 2015; Rybak et al. 2015a,b; Hezaveh et al. 2016). These studies led to the reconstruction of the matter distribution of the foreground lens through the detection of low-mass substructures, together with the pixelated surface brightness distribution of dust in the lensed source. Thanks to ALMA CO and CII spectroscopic data, it was also possible to measure with high precision the gas mass distribution and the kinematics of the clumps, revealing a disturbed morphology of the stellar, gas-and-dust components (see also Rybak et al. 2020). SDP.9 and SDP.11 ALMA high-resolution images of the continuum at 1.1 mm and of CO(6–5) (Wong et al. 2017) have been combined with X-ray band observations from Chandra to reconstruct the morphology and characterize the nuclear emission (Massardi et al. 2017).

2.2 ATCA follow-up

The sample in the H-ATLAS South Galactic Pole field comprises 30 sources with $22 < RA < 0$h and $-36 < \delta < -28$. All these are candidate, i.e. not yet confirmed, strongly lensed galaxies. Observations were centred at 2.1 GHz with a 2 GHz bandwidth and were carried out with the Australia Telescope Compact Array (ATCA) on 2017 December 14 and on 2019 July 31, respectively, with a 6 km and a 750 m east–west configurations. The corresponding largest angular scales (LAS) are 3.6 and 1.8 arcmin for the first and second configuration, respectively. The expected resolution is ∼10 arcsec if the farthest antenna, CA06, is included in the data, as in our case. In 2017, we got 12 allocated hours that allowed us to perform ∼7 × 2 min cuts on each target. In 2019, we performed 2 × 2 min at least on each source for a total of 4 observing hours. The observing strategy allowed enough coverage of the uv domain to recover suitable images of our targets. The weather and system conditions were excellent in both the observing epochs.

Data editing, calibration and imaging is performed using Miriad (Sault, Teuben & Wright 1995). Flagging of data is fully automatic and exploits the `PGFLAG` task, and calibration follows common procedures for 16 cm band data sets. Manual checking confirms that all the major RFI features are removed from the data, flagging more than 30 per cent of the data, but still recovering a 0.06 mJy beam^{-1} theoretical noise level (1σ). PKS1934-638 was observed as bandpass and flux calibrator. Two phase calibrators were observed during the 12 and 4 h observations (PKS0008-421 and PKS2255-282) and their solutions are merged to correct the data phases as a function of time.

The two data sets are combined during the imaging process with the task `UVAVER` in order to improve the uv-sampling and the dynamical range of the final image. We perform self-calibration during the imaging process in each observed field, exploiting the presence of several bright and point-like sources in the large field of view (22 arcmin FWHM), allowing the improvement of the overall signal-to-noise ratio. Flux densities ($S_{\rm image}$) and image noise ($\sigma_{\rm image}$) are then extracted from the Briggs-weighted continuum images with robust factor of 0.5. The average synthesized beam is ∼7.4 × 3.9 arcsec. Noise is computed as

$$\delta S_{\rm image} = \sqrt{(\sigma_{\rm image})^2 + (0.05 \times S_{\rm image})^2} \quad (2)$$

to consider the calibration errors. For later use, we convert the ATCA flux densities from 2.1 to 1.4 GHz assuming a power-law spectrum $S_\nu = \nu^\alpha$ with average radio spectral index $\alpha = -0.7 \pm 0.14$, consistently with Stacey et al. (2018).

2.3 FIRST catalogue counterparts

The FIRST (Faint Images of the Radio Sky at Twenty-cm; Becker, White & Helfand 1995) survey, performed with the VLA reaches a typical rms of 0.15 mJy beam $^{-1}$ and a resolution ∼5 arcsec comparable with those of our observations. FIRST overlaps with the Equatorial and North Galactic Pole H-ATLAS fields, thus complementing our search for radio counterparts for the Negrello et al. (2017) sample. The cross-match with the FIRST catalogue within 10 arcsec of the *Herschel*-ATLAS position yields 8 potential counterparts, while for 12 objects we find a clear $\gtrsim 3\sigma$ signal in the FIRST maps, within the H-ATLAS beamsize. For one of the matched source, namely H-ATLAS J142935.3-002836, the FIRST flux density value has been replaced with the more reliable one coming from the JVLA 7 GHz high-resolution (∼0.3 arcsec) and high-sensitivity (10 μJy beam^{-1}) observations described in Messias et al. (2014) (converted at 1.4 GHz).

Observations at 6.89 GHz from the JVLA are available for one additional source (H-ATLASJ133542.9+300401) and are described

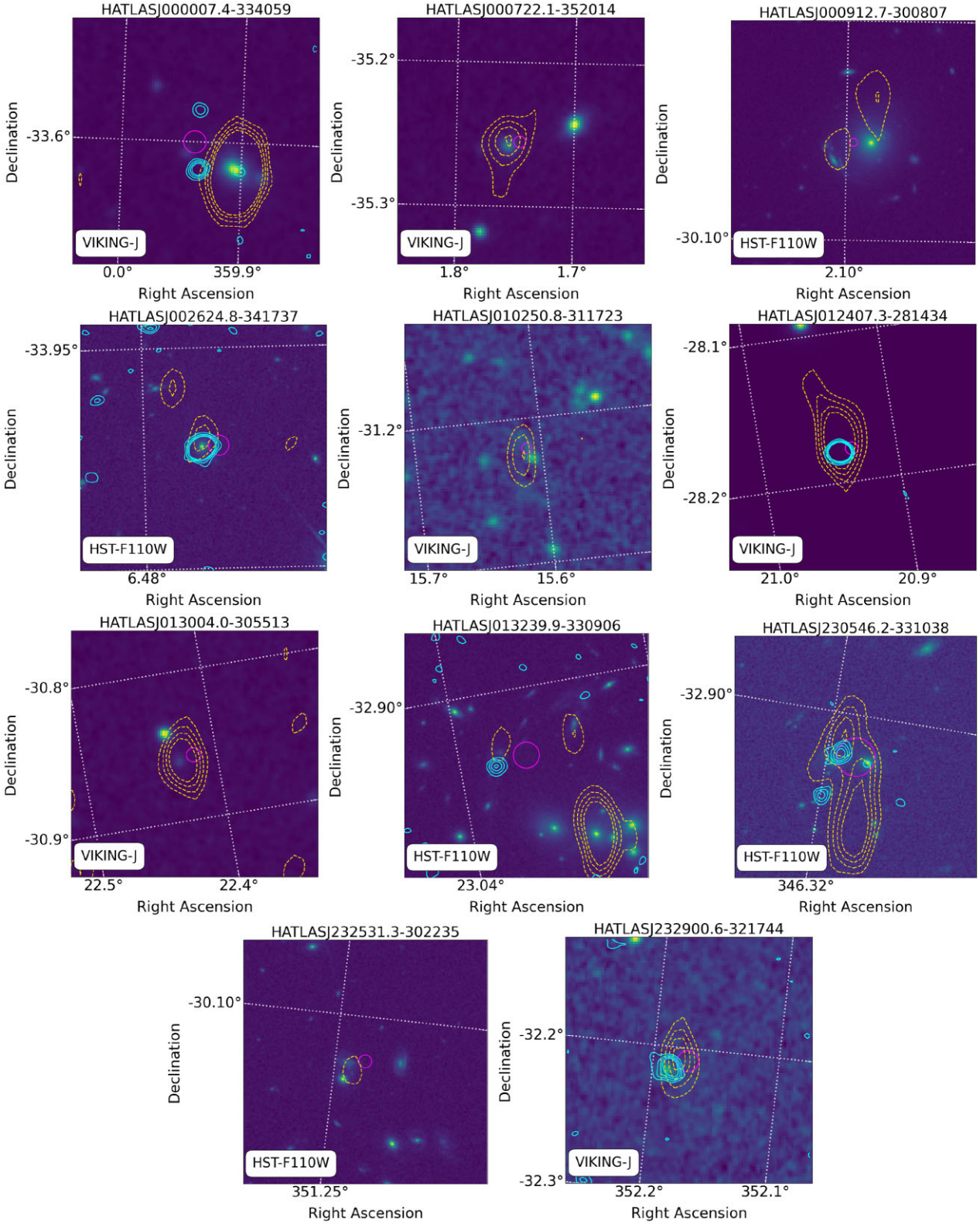

Figure 1. Cut-outs of NIR images with the best available angular resolution centred on the *Herschel* positions for the 11 sources with an ATCA cross-match. Contours at 3, 5, 7, 9σ levels are showed in gold for the radio and cyan for ALMA. Circles are the SPIRE position with a $3\sigma_{\rm pos}$ radius. RA and Dec. are reported in deg units. The postage stamps are 30x30 arcsec.

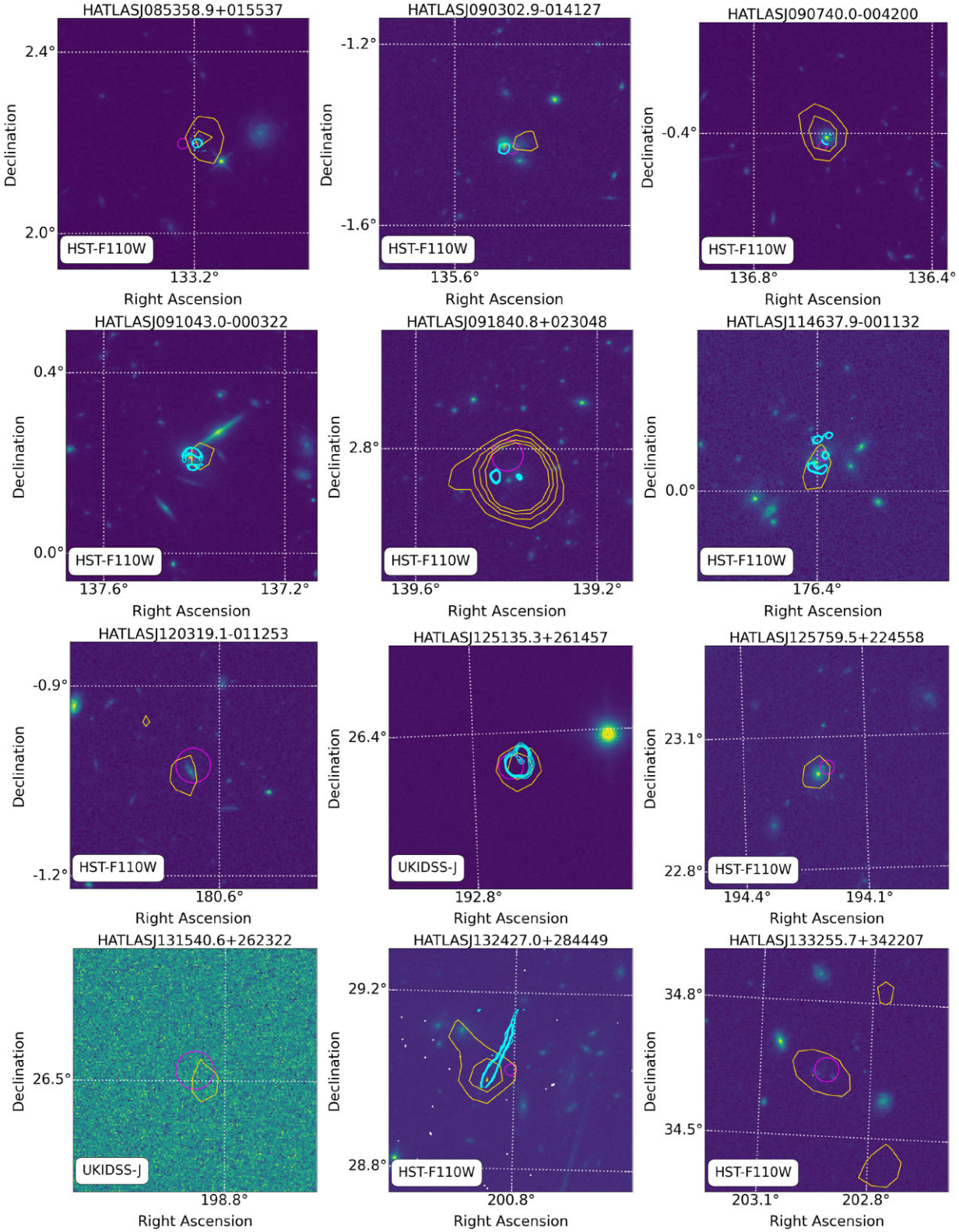

Figure 2. Cut-outs of NIR images with the best available angular resolution centred on the *Herschel* positions for the 16 sources with a FIRST cross-match. Contours at 3, 5, 7, 9σ levels are showed in gold for FIRST and cyan for ALMA. Circles are the SPIRE position with a $3\sigma_{\rm pos}$ radius. RA and Dec. are reported in deg units. The postage stamps are 30x30 arcsec.

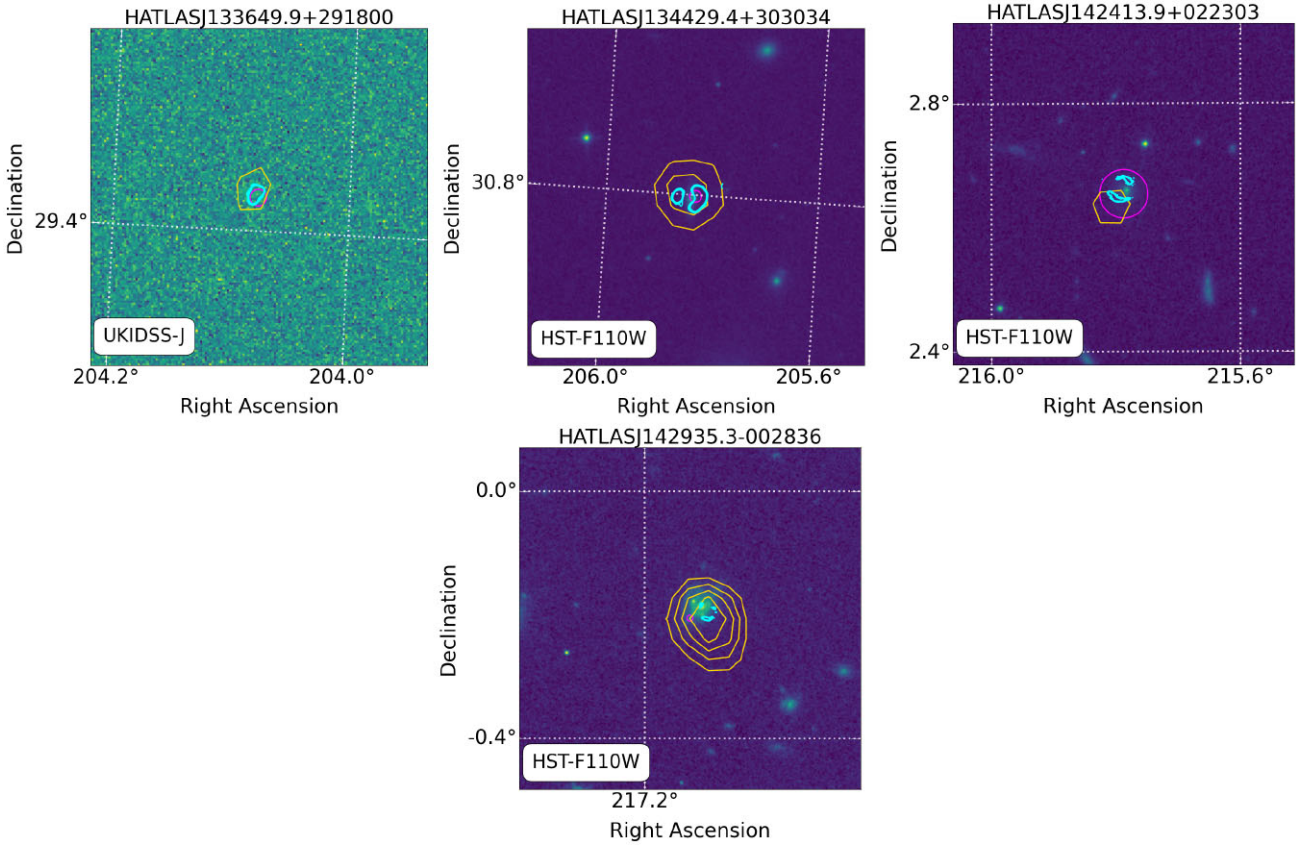

Figure 2 – *continued*

in details by Nayyeri et al. (2017). The image reaches an rms of 7.8 μJy beam^{-1} and a beam size of 1.01 × 0.81 arcsec; for our analysis, we use the flux density in the above paper already reported at 1.4 GHz (see table 1 in Nayyeri et al. 2017).

H-ATLASJ090311.6+003907 (SDP.81) is detected in the FIRST catalogue, was observed by the Extended Very Large Array (EVLA) at 8.4 GHz (Valtchanov et al. 2011; Rybak et al. 2015b). However, its radio emission is likely to be originated from the AGN hosted by the foreground lens (Tamura et al. 2015; Rybak et al. 2020); for this reason, it has been excluded a priori as a possible counterpart.

2.4 Counterparts selection

The detected sources display a variety of radio morphologies: some of them show a compact radio emission, others instead feature a more extended structure or even multiple components, but the angular resolution of the observations is not enough to resolve any of the arcs possibly associated with lensing effects.

For this reasons, in order to establish whether a radio source is correctly assigned as a counterpart of our selected *Herschel* sample, we selected radio detections with at least $>3\sigma_{\rm image}$ confidence level and then consider their position with respect to the optical/IR and the mm high angular resolution imaging.

We consider as a counterpart only the component nearest to the SPIRE peak position, whose radio-detected emission overlaps with sources detected the in NIR or mm, even though this can result in a underestimation of the radio luminosity in case of multiple component radio sources. In the NIR we exploit *HST*/WFC3 wide-J filter F110 maps described in Negrello et al. (2014) and more recent snapshot observations covering the Equatorial and Southern fields (PI: Marchetti 2019), both reaching an angular resolution of ∼0.13 arcsec. The remaining sources are observed by the UK Infrared Deep Sky Survey Large Area Survey (UKIDSS-LAS; Lawrence et al. 2007) and the VISTA Kilo-Degree Infrared Galaxy Survey (VIKING; Edge et al. 2013), reaching angular resolutions $\lesssim$1 arcsec. Millimetric the high-resolution images come from the ALMA Science Archive: some of the sources located in the South Galactic Pole have been target of Band 4 follow-ups at ∼1.7 arcsec, while for objects in the Northern and Equatorial fields we make use of the images found in bands 4, 6, and 7, with highest angular resolutions spanning from ∼1.2 to <0.1 arcsec. For sources without high-resolution imaging we compared the uncertainties on the radio positional accuracy (Becker et al. 1995) with respect to the one from SPIRE/250 μm (Bourne et al. 2011), with a ∼3σ tolerance. We include only objects showing a superimposition between the two centroids and/or between the SPIRE positional uncertainty and the radio detection.

Following the above criteria we find 11 and 17 sources in ATCA and FIRST, respectively, showed in Figs 1 and 2. Please note that the *HST*/WFC3 maps reported here do not take into account the well-known positional offset between ALMA and *HST* counterparts (Dunlop et al. 2016; Rujopakarn et al. 2016).

Therefore, combining ATCA follow-up and FIRST cross-matches we collected radio measurements for 28 out of the 80 galaxies in the original sample by Negrello et al. (2017), that will constitute our reference in this paper.

Table 1. Radio and FIR properties of the candidate and confirmed lensed galaxies with a counterpart in the radio bands. Columns are as follows: H-ATLAS IDs; *Herschel*/SPIRE flux densities; source redshift; lens classification from Negrello et al. (2017): (a) confirmed dusty lensed, (c) likely to be lensed, (c) uncertain; radio flux densities at 1.4 GHz; origin of the radio counterpart (images, catalogue, or literature); distance (in arcsec) of the radio peak from the *Herschel* position, if available.

#H-ATLAS ID	$S_{250\ \mu m}$ (mJy)	$S_{350\ \mu m}$ (mJy)	$S_{500\ \mu m}$ (mJy)	z[a]	Lenscode	$S_{1.4GHz}$ (mJy)	Counterpart	Dist (arcsec)
J000007.4−334059	130.3 ± 5.4	160.1 ± 5.9	116.2 ± 6.5	2.56 ± 0.43	C	1.91 ± 0.2	ATCA image	6.6
J000722.1−352014	237.3 ± 5.2	192.8 ± 5.6	107.5 ± 6.6	1.46 ± 0.3	C	0.39 ± 0.08	ATCA image	1.3
J000912.7−300807	352.8 ± 5.4	272.6 ± 6.1	156.1 ± 6.8	1.39 ± 0.29	C	0.20 ± 0.05	ATCA image	2.2
J002624.8−341737	137.7 ± 5.2	185.9 ± 5.8	148.8 ± 6.8	2.96 ± 0.48	C	0.26 ± 0.06	ATCA image	1.8
J010250.8−311723	267.9 ± 5.2	253.1 ± 5.7	168.1 ± 7.1	1.92 ± 0.35	C	0.29 ± 0.06	ATCA image	0.9
J012407.3−281434	257.5 ± 6	271.1 ± 6	203.9 ± 6.8	2.31 ± 0.4	C	0.79 ± 0.13	ATCA image	2.1
J013004.0−305513	164.4 ± 4.3	147.5 ± 5.1	100.6 ± 5.9	1.84 ± 0.34	C	0.65 ± 0.11	ATCA image	1.7
J013239.9−330906	112 ± 5.5	148.8 ± 6.2	117.7 ± 7	2.9 ± 0.47	C	0.19 ± 0.05	ATCA image	3.5
J085358.9+015537	396.4 ± 7.6	367.9 ± 8.2	228.2 ± 8.9	2.0925	A	1.19 ± 0.16	FIRST cat	2.0
J090302.9−014127(SDP.17)	354.1 ± 7.2	338.8 ± 8.1	220.2 ± 8.6	2.3049	A	0.41 ± 0.14	FIRST image	2.3
J090740.0−004200(SDP.9)	477.6 ± 7.3	327.9 ± 8.2	170.6 ± 8.5	1.577	A	1.21 ± 0.15	FIRST cat	2.1
J091043.0−000322(SDP.11)	420.8 ± 6.5	370.5 ± 7.4	221.4 ± 7.8	1.786	A	0.97 ± 0.19	FIRST image	1.3
J091840.8+023048	125.7 ± 7.2	150.7 ± 8.3	128.4 ± 8.7	2.581	C	4.63 ± 0.3	FIRST cat	2.2
J114637.9−001132	316 ± 6.6	357.9 ± 7.4	291.8 ± 7.7	3.259	A	1.14 ± 0.15	FIRST image	0.9
J120319.1−011253	114.3 ± 7.4	142.8 ± 8.2	110.2 ± 8.6	2.26 ± 0.39	C	0.82 ± 0.15	FIRST image	1.8
J125135.3+261457	157.9 ± 7.5	202.3 ± 8.2	206.8 ± 8.5	3.675	A	1.25 ± 0.16	FIRST cat	0.9
J125759.5+224558	272.4 ± 7.3	215 ± 8.1	137.8 ± 8.7	1.53 ± 0.3	B	0.85 ± 0.14	FIRST image	0.9
J131540.6+262322	94.1 ± 7.4	116.1 ± 8.2	108.6 ± 8.7	2.4417	C	0.96 ± 0.15	FIRST image	1.2
J132427.0+284449	342.4 ± 7.3	371 ± 8.2	250.9 ± 8.5	1.6760	A	1.95 ± 0.17	FIRST cat	3.9
J133255.7+342207	164.3 ± 7.5	186.8 ± 8.1	114.9 ± 8.7	2.9268	C	1.00 ± 0.16	FIRST image	1.9
J133542.9+300401	136.6 ± 7.2	145.7 ± 8.0	125.0 ± 8.5	2.685	A	0.14 ± 0.02	N17 obs	
J133649.9+291800	294.1 ± 6.7	286 ± 7.6	194.1 ± 8.2	2.2024	A	0.87 ± 0.15	FIRST image	1.2
J134429.4+303034	462 ± 7.4	465.7 ± 8.6	343.3 ± 8.7	2.301	A	1.29 ± 0.16	FIRST cat	0.6
J142413.9+022303	112.2 ± 7.3	182.2 ± 8.2	193.3 ± 8.5	4.243	A	0.79 ± 0.16	FIRST image	2.2
J142935.3−002836	801.8 ± 6.6	438.5 ± 7.5	199.8 ± 7.7	1.027	A	2.8 ± 0.67	M14	
J230546.2−331038	76.8 ± 5.6	110.9 ± 5.9	110.4 ± 7	3.67 ± 0.56	C	0.37 ± 0.07	ATCA image	2.8
J232531.3−302235	175.5 ± 4.3	227.0 ± 4.7	175.7 ± 5.7	2.8 ± 0.46	C	0.105 ± 0.03	ATCA image	1.9
J232900.6−321744	118.3 ± 4.7	141.2 ± 5.2	119.7 ± 6.4	2.81 ± 0.46	C	0.31 ± 0.06	ATCA image	1.6

Note. N17: Nayyeri et al. (2017), M14: Messias et al. (2014); [a]spectroscopic redshifts of H-ATLASJ130333.1+244643, H-ATLASJ131540.6+262322, and H-ATLASJ133255.7+342207 are taken from Neri et al. (2020).

For the remaining objects, we define an upper limit for detection at 3σ from the noise at the position of the sources in the FIRST images and as $3\sigma_{\rm image}$ for ATCA images. Table 1 summarizes the radio and FIR photometry for our sample.

Finally, few considerations need to be done. First, we would like to stress that in this paper we rely only on the available archived radio data without focusing into descriptions of the single objects. In our analysis, we take into account the information available in the literature for the confirmed cases, but for the remaining unconfirmed ones in absence of an accurate lens modelling and/or higher angular resolution observations, it is not possible to confirm whether or in which fraction the radio emission is associated to the lensed object. This is also valid for the SPIRE flux densities in the unconfirmed cases. Indeed, as showed in Figs 1 and 2, multiple sources entering the *Herschel* beam are detected in the ALMA (sub-)mm maps, leading to a possible overestimation of the effective FIR luminosity of the actual counterpart. A fraction of low-resolution sub-mm detected sources is indeed expected to be composed by multiple ALMA sources (Hodge et al. 2013; Smail & Walter 2014; Bussmann et al. 2015). Here, we assume that the observed SPIRE flux density is mostly originated by the same object and that no strong FIR contamination from possible nearby sources is present. In any case, this should not affect the objects already confirmed to be lensed. In fact, we expect the FIR luminosity of the lensed galaxies in our sample to be magnified by a factor spanning the range ∼3–10 (Negrello et al. 2017; Enia et al. 2018), with a negligible contribution from possible additional unlensed sources entering the *Herschel* beam.

2.5 Physical properties of the sample

The rest-frame radio luminosity $L_{1.4GHz}$ at 1.4 GHz for each source (see Table 2) is computed as

$$L_{\nu,e} = \frac{4\pi D_L^2(z)}{(1+z)^{1+\alpha}} \left(\frac{\nu_e}{\nu_o}\right)^{\alpha} S_{\nu,o}, \quad (3)$$

where $S_\nu \propto \nu^\alpha$ is the monochromatic flux density at a certain frequency and α is assumed to be -0.7 as the typical value at 1.4 GHz for FIRST (Kimball & Ivezić 2008), ν_e and ν_o are the emitted and the observed frequency, and $D_{\rm L}$ is the luminosity distance computed for each redshift according to the adopted ΛCDM cosmology. Our 28 objects span a range $1.9 \times 10^{24} \lesssim L_{1.4GHz} \lesssim 1.8 \times 10^{26}$ W Hz^{-1} (uncorrected for the lens magnification factor μ), with a median value of $L_{1.4GHz} \sim 2.4 \times 10^{25}$ W Hz^{-1}.

The FIR luminosity $L_{\rm FIR}$ (see Table 2) is computed for each source in the main sample of Negrello et al. (2017) by fitting the *Herschel*/SPIRE photometry described in Section 2.1. We use a single-temperature modified blackbody under the optically thin approximation with dust emissivity index $\beta = 1.5$ (Nayyeri et al. 2016; Negrello et al. 2017), the spectrum normalization and the dust temperature ($T_{\rm dust}$) are kept as free parameters. The model ($S_{\nu,\,\rm best}$) that minimizes the χ^2 is then integrated over the wavelength range

Table 2. 1.4 GHz and FIR luminosities (*uncorrected* for lensing magnification effects) and q_{FIR} parameter for the 28 galaxies in our sample.

#H-ATLAS ID	$\log(L_{1.4GHz})$ $[L_\odot]$	$\log(L_{FIR})$ $[W\ Hz^{-1}]$	q_{FIR}
J000007.4−334059	25.86 ± 0.04	13.40 ± 0.05	1.55 ± 0.15
J000722.1−352014	24.62 ± 0.06	13.11 ± 0.02	2.49 ± 0.13
J000912.7−300807	24.29 ± 0.10	13.24 ± 0.01	2.96 ± 0.23
J005132.8−301848	25.13 ± 0.08	13.59 ± 0.07	2.47 ± 0.24
J010250.8−311723	24.77 ± 0.07	13.41 ± 0.03	2.64 ± 0.17
J012407.3−281434	25.37 ± 0.05	13.58 ± 0.04	2.20 ± 0.14
J013004.0−305513	25.07 ± 0.05	13.15 ± 0.03	2.08 ± 0.12
J013239.9−330906	24.98 ± 0.10	13.48 ± 0.07	2.50 ± 0.28
J085358.9+015537	25.46 ± 0.06	13.68 ± 0.03	2.22 ± 0.14
J090302.9−014127	25.09 ± 0.15	13.72 ± 0.03	2.64 ± 0.35
J090740.0−004200	25.19 ± 0.05	13.57 ± 0.01	2.39 ± 0.12
J091043.0−000322	25.22 ± 0.08	13.55 ± 0.02	2.33 ± 0.20
J091840.8+023048	26.25 ± 0.02	13.39 ± 0.06	1.14 ± 0.15
J114637.9−001132	25.86 ± 0.06	14.03 ± 0.05	2.17 ± 0.18
J120319.1−011253	25.54 ± 0.08	13.40 ± 0.06	1.86 ± 0.23
J125135.3+261457	26.01 ± 0.05	13.87 ± 0.09	1.86 ± 0.23
J125759.5+224558	25.01 ± 0.07	13.21 ± 0.02	2.20 ± 0.17
J131540.6+262322	25.51 ± 0.07	13.21 ± 0.07	1.70 ± 0.23
J132427.0+284449	25.46 ± 0.04	13.37 ± 0.04	1.91 ± 0.12
J133255.7+342207	25.42 ± 0.07	13.33 ± 0.04	1.92 ± 0.18
J133542.9+300401	24.75 ± 0.07	13.45 ± 0.05	2.70 ± 0.20
J133649.9+291800	25.37 ± 0.07	13.59 ± 0.03	2.22 ± 0.18
J134429.4+303034	25.59 ± 0.05	13.83 ± 0.04	2.24 ± 0.15
J142413.9+022303	25.95 ± 0.09	13.93 ± 0.12	1.99 ± 0.34
J142935.3−002836	25.13 ± 0.10	13.57 ± 0.01	2.44 ± 0.23
J230546.2−331038	25.49 ± 0.06	13.58 ± 0.1	2.10 ± 0.27
J232531.3−302235	24.69 ± 0.11	13.63 ± 0.06	2.95 ± 0.30
J232900.6−321744	25.15 ± 0.06	13.45 ± 0.06	2.30 ± 0.19

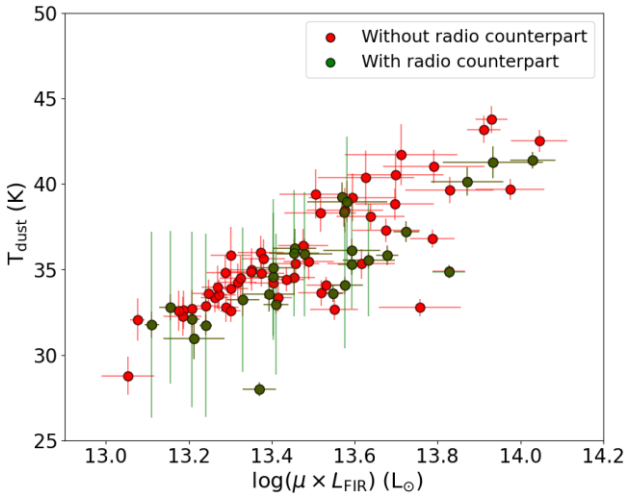

Figure 3. Dust temperatures versus FIR luminosities (uncorrected for magnification) for the 80 (candidate) strongly lensed galaxies from Negrello et al. (2017). Green and red dots show, respectively, sources with and without radio counterpart.

8–1000 μm as follows:

$$L_{FIR} = \frac{4\pi D_L^2}{(1+z)} \int_{8\mu m}^{1000\mu m} S_{\nu,best} d\nu. \quad (4)$$

The resulting FIR luminosities (uncorrected for lens magnification) and dust temperatures are showed in Fig. 3. The FIR luminosities span the range $1.3 \times 10^{13} \lesssim L_{FIR} \lesssim 1.1 \times 10^{14} L_\odot$, with a median value of $L_{FIR} \sim 3.5 \times 10^{13} L_\odot$. The median value of the dust temperature for the total sample of candidate strongly lensed galaxies is $T_{dust} = 35.2 \pm 2.1$, consistently with what was found by Negrello et al. (2017) for the same sample.

3 THE FIR-RADIO CORRELATION FOR (CANDIDATE) LENSED GALAXIES

In this section, we explore the correlation between the radio and the FIR luminosities for our sample of 28 (candidate) lensed dusty star-forming galaxies, focusing on the observed quantities uncorrected for lensing magnification effects. For each galaxy, we computed the q_{FIR} parameter following equation (1).

Fig. 4 shows the q_{FIR} parameter as a function of redshift. We find a weak yet appreciable decline of q_{FIR} with increasing z. Our result is compared with the redshift evolution reported by Magnelli et al. (2015) and Delhaize et al. (2017) (red and green-shaded areas, respectively) and with the median value of the q_{FIR} parameter for star-forming radio galaxies from Ivison et al. (2010b). Magnelli et al. (2015) studied a mass-selected sample of star-forming galaxies up to $z \sim 2$, finding a slight evolution $q_{FIR}(z) = (2.35 \pm 0.08)(1+z)^{-0.12 \pm 0.04}$; in Fig. 4, their relation is extended up to higher redshifts to ease the comparison with our data. Similar results were obtained by Delhaize et al. (2017) from a radio-selected sample of star-forming galaxies extending up to $z \sim 6$, as described by the relation $q_{FIR}(z) = (2.52 \pm 0.03)(1+z)^{-0.21 \pm 0.01}$. The majority of our sources show values of q_{FIR} within the 2σ interval around the median value of Ivison et al. (2010b) for star-forming galaxies. Three sources lie below the limit of $q_{FIR} \sim 1.8$ established by Condon et al. (2002) to separate between sources with radio emission powered by star formation and by AGN, respectively. The AGN-powered objects are all located at redshifts $z \gtrsim 2$.

Fig. 5 shows the dependence of the q_{FIR} parameter on the radio luminosity (uncorrected for lensing magnification). We find a clear tendency of the q_{FIR} parameter to decrease with increasing radio power. The radio excess follows from the definition given in equation (1) and, consequently, this observed trend can be ascribed to the presence of an AGN. Such a behaviour is similar to what have been revealed by Stacey et al. (2018) observing a sample of strong gravitationally lensed quasars. Their sample includes 104 quasars lensed by foreground galaxies, listed in the SQLS catalogue and CASTLES data base (Kochanek et al. 1999; Munoz et al. 1999; Inada et al. 2012) and detected in a variety of optical and radio surveys. For clarity, we report in the figure their 31 detected sources that could be divided in three categories: jetted quasars, where high-resolution radio data confirmed the emission to be associated with AGN jets; non-jetted quasars, dominated by radio emission triggered by star formation; quasars where the origin of the radio emission is unknown. They assumed a magnification factor of $\mu = 10^{+10}_{-5}$ for the majority of their sample, and the estimated median value of the total infrared luminosity amounts to $3.6^{+4.8}_{-2.4} x 10^{11}\ L_\odot$. Two additional sources are the gravitationally lensed radio-quiet quasars targeted by the LOFAR Two-metre Sky Survey (LoTSS) and detected by *Herschel* described in Stacey et al. (2019).

19 out of the 31 detected lensed quasars from Stacey et al. (2018) are located below the threshold of 1.8 and are mostly (with only one exception) classified as jet-dominated. For the remaining sources, only two quasars are confirmed to be star formation-dominated sources and are found to be above the 1.8 threshold within their uncertainties. The nature of the radio emission of the remaining one-third of the sample (10 sources) is still uncertain. Only the 25 per cent

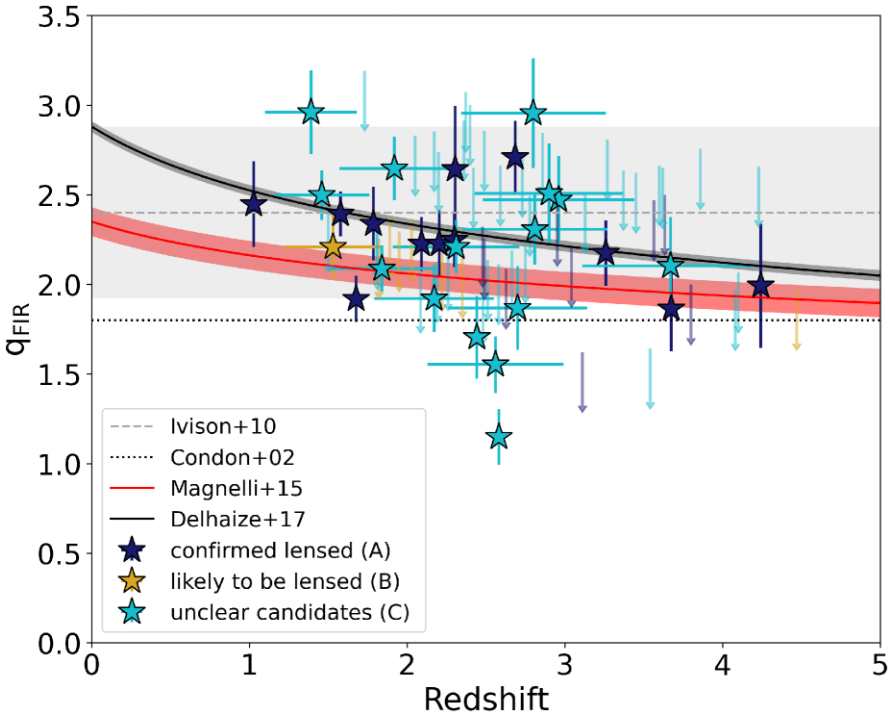

Figure 4. q_{FIR} parameter (see equation 1) as a function of redshift. The grey-dashed line corresponds to the median q_{FIR} for star-forming galaxies as defined by Ivison et al. (2010b), the grey-shaded area represents the 2σ dispersion. Red- and black-shaded areas represent, respectively, the relation by Magnelli et al. (2015) and Delhaize et al. (2017). Stars are the 28 galaxies in our sample: (blue) the confirmed lensed objects, (yellow) the likely lensed objects, and (cyan) the uncertain objects. Arrows show the 3σ upper limits for the remaining undetected sources.

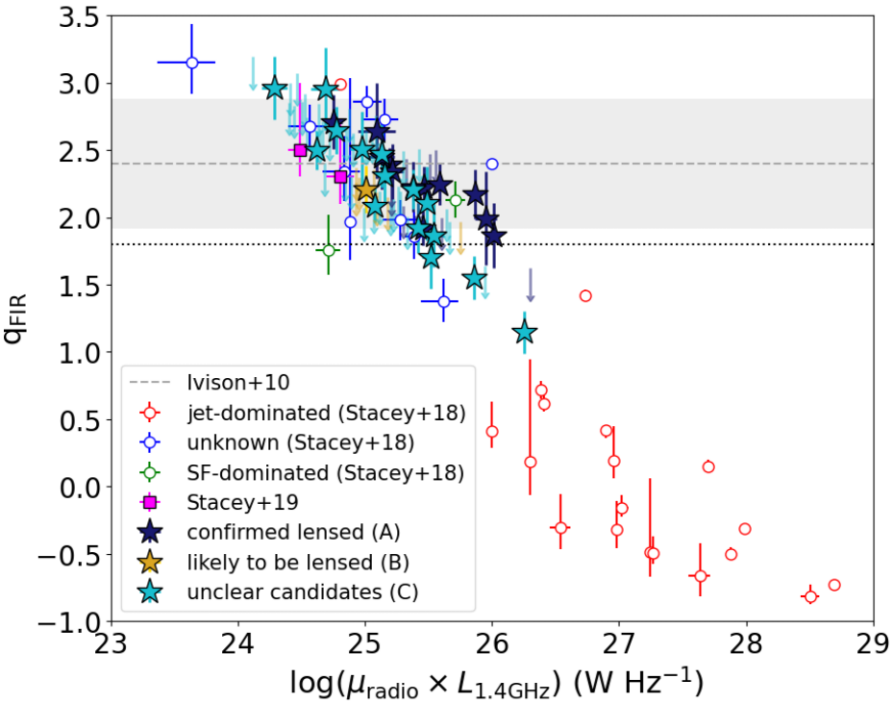

Figure 5. The q_{FIR} parameter, computed using the FIR luminosity, as a function of the logarithm of the 1.4 GHz luminosity (not corrected for lens magnification). Circles are the Stacey et al. (2018) lensed quasars classified according to the origin of their radio emission: (red) jets, (green) star formation, and (blue) unknown. Squares are from Stacey et al. (2019). Arrows show the 3σ upper limits for the remaining undetected sources.

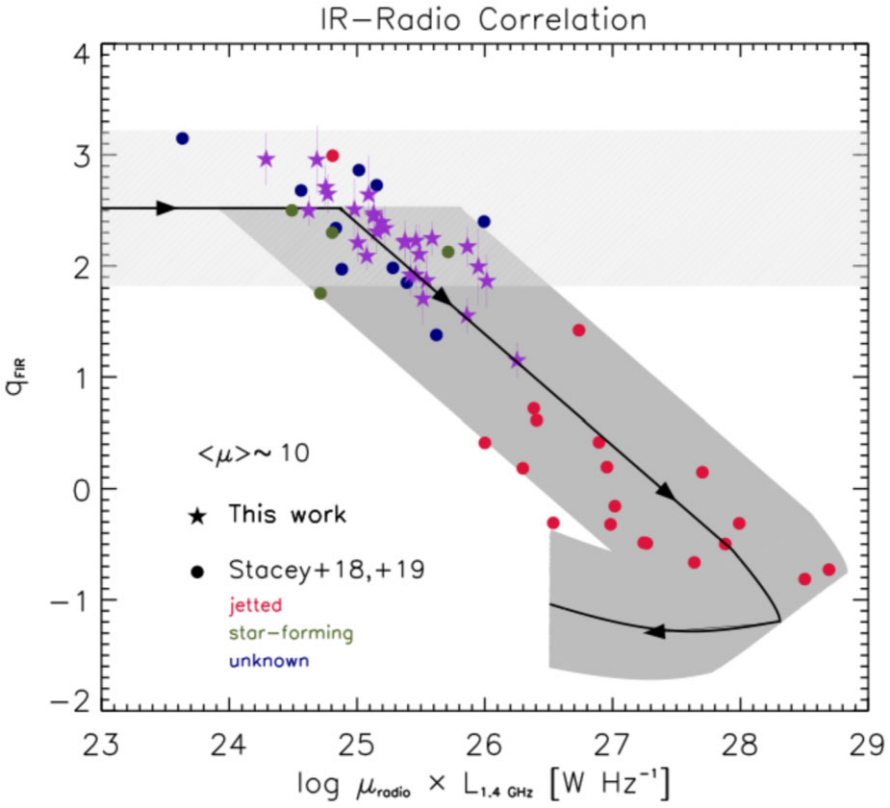

Figure 6. The FIR–radio correlation in terms of the $q_{\rm FIR}$ versus radio luminosity (uncorrected for lensing magnification). Data from this work (stars) and from Stacey et al. (2018, 2019). Circles: red for jetted source, green for star-forming galaxies and blue for uncertain ones) are compared with the prediction of the *in situ* galaxy formation scenario by Lapi et al. (2014), Lapi et al. (2018) for radio loud AGNs. Specifically, the dark grey area represent the locus of radio-loud AGNs and the light shaded area that for star-forming galaxies without a significant AGN contribution to the radio emission. The black line with arrows illustrates the typical evolution of an individual radio-loud AGN at $z \sim 2$. An average magnification $\langle\mu\rangle \sim 10$ (as estimated by Stacey et al. 2018) has been applied to the model predictions for fair comparison with the data of gravitationally lensed sources.

of their sample has $q_{\rm FIR} < 1.8$ and lie in the same region of the jet-dominated quasars of Stacey et al. (2018), actually aligning on to their trend of $q_{\rm FIR}$ with radio luminosity. Most relevantly, the majority of our sources lie ($\sim$ 90 per cent) in the region where radio emission is dominated by star formation, thus complementing the radio/optical selection adopted in Stacey et al. (2018) and actually extending to lower radio luminosities a consistent $q_{\rm FIR}$ versus radio luminosity relation.

Finally, our assumption that the FIR luminosity is not strongly affected by nearby objects entering the *Herschel* beam is reasonable. If not, the trend in Fig. 5 should show a clear offset with respect to the confirmed lensed galaxies and/or with the points from Stacey et al. (2018, 2019). Another support to this assumption is given by the fact that our points are consistent within the uncertainties with the span of the $q_{\rm FIR}$–$L_{1.4\rm GHz}$ relation.

4 PHYSICAL INTERPRETATION

In the way of providing a physical interpretation, in Fig. 6 we compare the observed FIR-radio correlation from this work and from Stacey et al. (2018, 2019) to the *in situ* galaxy formation scenario by Lapi et al. (2014, 2018) (see also Mancuso et al. 2017; Pantoni et al. 2019). This scenario envisages star formation and (super)massive black hole (BH) accretion in galaxies to be essentially in situ and time-coordinated processes, triggered by the fast collapse of baryons in the host dark-matter haloes and subsequently controlled by self-regulated baryonic physics, in particular by energy/momentum feedback from SNe and from the central active nucleus.

The evolution of an individual massive galaxy (say the high-redshift star-forming progenitor of a present-day elliptical) predicted by the model consists of different stages (see Lapi et al. 2018, their Fig. 1 for a schematic illustration). Early on, the balance between cooling, infall, compaction, and stellar feedback processes sets in a strong and dust-enshrouded star formation activity (SFR $\sim$ several 10^2 $M_\odot$ yr^{-1}), with a roughly constant behaviour in time (stellar mass increases almost linearly). Meanwhile, in the inner, gas-rich galaxy regions the central BH undergoes an exponential growth in Eddington-limited conditions. In this stage, the system behaves as a bright IR/(sub)mm galaxy with an X-ray active nucleus. When the central BH has grown to a significant mass, its energy output becomes so large as to eject gas and dust from the host and eventually quench the star formation and reduce the accretion on to itself to sub-Eddington values. In this stage, the system behaves as a powerful AGN with possible residual star formation. Thereafter, the stellar population evolves almost passively, and the system behaves as a red and dead massive quiescent galaxy; its further evolution in mass and size towards the present is mainly due to minor dry merger events.

In the early stages of the evolution when the central BH is still small and the nuclear power quite limited, the radio emission is mostly associated to the star formation in the host, implying modest $L_{1.4\,\rm GHz}$ and standard values $q_{\rm FIR} \approx 2.5$. Later on, when the BH mass has increased to substantial values, the radio emission from the nucleus

progressively overwhelms that from the star formation, driving $q_{\rm FIR}$ toward values appreciably smaller than 2.5. Values smaller even than 1.8 are obtained when jetted emission is produced, preferentially in the late-stage of the evolution: this is because extraction of rotational energy to drive jets is favoured in sub-Eddington conditions that sets in when the gaseous environment around the BH has been partially cleaned by the feedback from the nucleus itself (see above).

The typical model evolutionary track of a radio-loud AGN in the $q_{\rm FIR}$ versus radio luminosity diagram is illustrated by the black line with arrows in Fig. 6; the dark shaded area is the locus expected for such objects taking into account the relative contribution of sources with different masses, weighted by their statistics and timescales. For reference, the light-shaded area refers to the typical $q_{\rm FIR}$ parameter of a star-forming galaxies with negligible contribution from AGNs to the radio emission. The agreement of the model prediction with the data is pleasingly good, and testifies that the behaviour of the FIR-radio correlation is physically driven by the onset of jetted radio emission, and consistent with a co-evolution scenario between star formation and BH growth. A further, more detailed comparison between such a scenario and data will be pursued in a forthcoming paper, where we will estimate physical quantities (e.g. SFR, stellar mass, and stellar ages) for the galaxy sample presented in this work via broadband spectral energy distribution fitting.

5 CONCLUSIONS

Our analysis exploited the FIR-selected, *Herschel*-ATLAS (H-ATLAS) candidate strongly lensed galaxy sample by Negrello et al. (2017) to investigate the FIR-radio correlation out to redshift $z \sim 4$. Specifically:

(i) We cross-matched the Negrello et al. (2017) sample with the FIRST survey at 1.4 GHz and run dedicated follow-up with ATCA at 2.1 GHz, finding 11 and 16 matches, respectively; the addition of another source observed at ∼7 GHz with the JVLA (analysed in detail by Nayyeri et al. 2017) leaded us to a sample of 28 candidate lensed dusty star-forming galaxies with a radio counterpart over the redshift range $1 \lesssim z \lesssim 4$.

(ii) We derived the radio and the integrated FIR luminosities for the selected sample (uncorrected for lensing magnification), that feature radio luminosities in the range $1.9 \times 10^{24} \lesssim L_{1.4\,\rm GHz}$ [W Hz^{-1}] $\lesssim 1.8 \times 10^{26}$ and integrated FIR luminosity in the range $1.3 \times 10^{13} \lesssim L_{\rm FIR}/{\rm L}_{\odot} \lesssim 1.1 \times 10^{14}$.

(iii) By taking advantage of the source brightness possibly enhanced by lensing magnification we identified a weak evolution with redshift out to $z \lesssim 4$ of the FIR-to-radio luminosity ratio $q_{\rm FIR}$, consistent with previous determinations at lower redshift based on different selections.

(iv) We found that the $q_{\rm FIR}$ parameter as a function of the radio power $L_{1.4\,\rm GHz}$ displays a clear decreasing trend, similarly to the lensed quasars selected in optical/radio by Stacey et al. (2018), yet covering a complementary region in the $q_{\rm FIR} - L_{1.4\,\rm GHz}$ diagram.

(v) We interpreted the behaviour of the FIR–radio correlation according to an *in situ* galaxy evolution scenario, as the result of the transition from an early dust-obscured star-forming phase (mainly pinpointed by our FIR selection) to a late radio-loud quasar phase (preferentially sampled by the Stacey et al. 2018 selection).

ACKNOWLEDGEMENTS

This paper makes use of the following ALMA data: 2013.1.00164.S, 2013.1.00358.S, 2015.1.00415.S, 2015.1.01455.S, 2016.1.00282.S, 2016.1.00450.S, 2017.1.00027.S, 2018.1.00526.S, and 2019.1.01477.S. ALMA is a partnership of ESO (representing its member states), NSF (USA) and NINS (Japan), together with NRC (Canada), MOST and ASIAA (Taiwan), and KASI (Republic of Korea), in cooperation with the Republic of Chile. The Joint ALMA Observatory is operated by ESO, AUI/NRAO, and NAOJ. We acknowledge financial support from the grant PRIN MIUR 2017 prot. 20173ML3WW 001 and 002 'Opening the ALMA window on the cosmic evolution of gas, stars, and supermassive black holes'. AL is supported by the EU H2020-MSCAITN-2019 project 860744 'BiD4BEST: Big Data applications for Black hole Evolution STudies'. We acknowledge the referee, J. P. McKean, for the useful comments.

DATA AVAILABILITY

The data underlying this article are the following:

(i) The public catalogue of 80 candidate gravitationally lensed galaxies extracted from the full H-ATLAS survey, published by Negrello et al. (2017).

(ii) The *Herschel*/SPIRE images at 250 μm, produced from the H-ATLAS DR2 maps (https://www.h-atlas.org/public-data/download).

(iii) The Australian Telescope Compact Array data products from the Australia Telescope Online Archive, publicly available at the following link: https://atoa.atnf.csiro.au/query.jsp, project code: C3215.

(iv) The last version of the Very Large Array FIRST survey catalogue (2014 Dec 14, Helfand, White & Becker 2015), accessible through VizieR: https://vizier.u-strasbg.fr/viz-bin/VizieR-3.

(v) The Very Large Array FIRST survey maps extracted from the cutout service available at the following link: https://third.ucllnl.org/cgi-bin/firstcutout.

(vi) *HST* images taken from MAST: Barbara A. Mikulski Archive for Space Telescopes, https://mast.stsci.edu/.

(vii) VIKING and UKIDSS-LAS cutouts, generated from https://alasky.u-strasbg.fr/hips-image-services/hips2fits.

(viii) ALMA images available in the ALMA Science Archive, project codes for the adopted images are 2013.1.00164.S, 2013.1.00358.S, 2015.1.00415.S, 2015.1.01455.S, 2016.1.00282.S, 2016.1.00450.S, 2017.1.00027.S, 2018.1.00526.S, and 2019.1.01477.S.

REFERENCES

Algera H. S. B. et al., 2020, ApJ, 903, 138
An F. et al., 2021, MNRAS, 507, 2643
Basu A., Wadadekar Y., Beelen A., Singh V., Archana K. N., Sirothia S., Ishwara-Chandra C. H., 2015, ApJ, 803, 51
Becker R. H., White R. L., Helfand D. J., 1995, ApJ, 450, 559
Blain A. W., Smail I., Ivison R. J., Kneib J. P., Frayer D. T., 2002, Phys. Rep., 369, 111
Bonato M. et al., 2021, A&A, 656, A48
Bourne N., Dunne L., Ivison R. J., Maddox S. J., Dickinson M., Frayer D. T., 2011, MNRAS, 410, 1155
Bussmann R. S. et al., 2013, ApJ, 779, 25
Bussmann R. S. et al., 2015, ApJ, 812, 43
Calistro Rivera G. et al., 2017, MNRAS, 469, 3468
Condon J. J., Cotton W. D., Broderick J. J., 2002, AJ, 124, 675
Delhaize J. et al., 2017, A&A, 602, A4
Delvecchio I. et al., 2020, A&A, 647, A123
Dunlop J. S. et al., 2016, MNRAS, 466, 861
Dye S. et al., 2015, MNRAS, 452, 2258

Eales S. et al., 2010, PASP, 122, 499
Edge A., Sutherland W., Kuijken K., Driver S., McMahon R., Eales S., Emerson J. P., 2013, Messenger, 154, 32
Enia A. et al., 2018, MNRAS, 475, 3467
Hatsukade B., Tamura Y., Iono D., Matsuda Y., Hayashi M., Oguri M., 2015, PASJ, 67, 93
Helfand D. J., White R. L., Becker R. H., 2015, Apj, 801, 26
Helou G., Soifer B. T., Rowan-Robinson M., 1985, ApJ, 298, L7
Hezaveh Y. D. et al., 2016, ApJ, 823, 37
Hodge J. A. et al., 2013, ApJ, 768, 91
Inada N. et al., 2012, ApJ, 143, 119
Ivison R. J. et al., 2010a, MNRAS, 402, 245
Ivison R. J. et al., 2010b, A&A, 518, L31
Jarvis M. J. et al., 2010, MNRAS, 409, 92
Jarvis M. J. et al., 2015, in Advancing Astrophysics with the Square Kilometre Array (AASKA14). preprint (arXiv:1412.5753)
Jarvis M. J. et al., 2016, in MeerKAT Science: On the Pathway to the SKA. preprint (arXiv:1709.01901)
Kennicutt R. C., Evans N. J., 2012, ARA&A, 50, 531
Kimball A. E., Ivezić, Ž., 2008, ApJ, 136, 684
Kochanek C. S., Falco E. E., Impey C. D., Lehaár J., McLeod B. A., Rix H.-W., 1999, in Holt S., Smith E., eds, The 9th Astrophysics Conference: After the Dark Ages, When Galaxies were Young (the Universe at 2). Vol. 470, AIP Conf. Proc., Am. Inst. Phys., New York, p. 163
Lacki B. C., Thompson T. A., 2010, ApJ, 717, 196
Lapi A. et al., 2018, ApJ, 857, 22
Lapi A., Raimundo S., Aversa R., Cai Z. Y., Negrello M., Celotti A., De Zotti G., Danese L., 2014, ApJ, 782, 69
Lawrence A. et al., 2007, MNRAS, 379, 1599
Madau P., Dickinson M., 2014, ARA&A, 52, 415
Maddox S. J. et al., 2017, ApJ, 236, 30
Magnelli B. et al., 2015, A&A, 573, A45
Mancuso C. et al., 2017, ApJ, 842, 95
Massardi M. et al., 2017, A&A, 610, A53
Messias H. et al., 2014, A&A, 568, A92
Molnár D. C. et al., 2017, MNRAS, 475, 827
Molnár D. C. et al., 2021, MNRAS, 504, 118
Munoz J. A., Falco E. E., Kochanek C. S., Lehar J., McLeod B. A., Impey C. D., Rix H. W., Peng C. Y., 1999, Ap&SS, 263, 51
Murphy E. J., 2009, ApJ, 706, 482
Murphy E. J., 2019, Proc. Int. Astron. Union, 15, 177
Nayyeri H. et al., 2016, ApJ, 823, 17
Nayyeri H. et al.,2017, ApJ, 844, 82
Negrello M. et al., 2010, Science, 330, 800
Negrello M. et al., 2014, MNRAS, 440, 1999
Negrello M. et al., 2017, MNRAS, 465, 3558
Neri R. et al., 2020, A&A, 635, A7
Novak M. et al., 2017, A&A, 602, A5
Ocran E. F., Taylor A. R., Vaccari M., Ishwara-Chandra C. H., Prandoni I., Prescott M., Mancuso C., 2020, MNRAS, 491, 5911
Oliver S. J. et al., 2012, MNRAS, 424, 1614
Pantoni L. et al., 2021, MNRAS, 507, 3998
Pantoni L., Lapi A., Massardi M., Goswami S., Danese L., 2019, ApJ, 880, 129
Partnership A. et al., 2015, ApJ, 808, L4
Planck Collaboration VI, 2020, A&A, 641, A6
Rujopakarn W. et al., 2016, ApJ, 833, 12
Rybak M., Hodge J. A., Vegetti S., van der Werf P., Andreani P., Graziani L., McKean J. P., 2020, MNRAS, 494, 5542
Rybak M., McKean J. P., Vegetti S., Andreani P., White S. D. M., 2015a, MNRAS, 451, L40
Rybak M., Vegetti S., McKean J. P., Andreani P., White S. D. M., 2015b, MNRAS, 453, L26
Sargent M. T. et al., 2010, ApJ, 714, L190
Sault R. J., Teuben P. J., Wright M. C. H., 1995, in Shaw R. A., Payne H. E., Hayes J. J. E., eds, ASP Conf. Ser. Vol. 77, Astronomical Data Analysis Software and Systems IV. Astron. Soc. Pac., San Francisco, p. 433
Schleicher D. R. G., Beck R., 2016, A&A, 593, A77
Smail I., Walter F., 2014, Messenger, 157, 41
Smith D. J. B. et al., 2014, MNRAS, 445, 2232
Smith D. J. B. et al., 2021, A&A, 648, A6
Sopp H. M., Alexander P., 1991, MNRAS, 251, 14P
Stacey H. R. et al., 2018, MNRAS, 476, 5075
Stacey H. R. et al., 2019, A&A, 622, A18
Swinbank A. M. et al., 2015, ApJ, 806, L17
Tabatabaei F. S. et al., 2016, ApJ, 836, 185
Tamura Y., Oguri M., Iono D., Hatsukade B., Matsuda Y., Hayashi M., 2015, PASJ, 67, 72
Thomson A. P. et al., 2014, MNRAS, 442, 577
Valiante E. et al., 2016, MNRAS, 462, 3146
Valtchanov I. et al., 2011, MNRAS, 415, 3473
Viero M. P. et al., 2014, ApJS, 210, 22
Wang L. et al., 2019, A&A, 631, A109
Wardlow J. L. et al., 2013, ApJ, 762, 59
Wong K. C., Ishida T., Tamura Y., Suyu S. H., Oguri M., Matsushita S., 2017, ApJ, 843, L35
Yun M. S., Reddy N. A., Condon J. J., 2001, ApJ, 554, 803

This paper has been typeset from a TEX/LATEX file prepared by the author.